

Two facilitating mechanisms for SF₆ streamer breakdown induced by a floating linear metal particle: equivalent pulsed streamer (EPS) and side streamer (SS)

Zihao Feng,¹ Liyang Zhang,¹ Xinxin Wang,¹ Xiaobing Zou,¹ and Haiyun Luo¹

¹Department of Electrical Engineering, Tsinghua University, Beijing 100084, China

The electrical breakdown of SF₆ in the presence of floating metal particles is facilitated by two key factors: the role of floating metal particles and the nonlinear breakdown behavior of high-pressure SF₆. However, the microscopic transient processes remain unclear, motivating this paper. Using 2D fluid models, we investigate SF₆ streamer breakdown induced by a floating linear metal particle under negative applied voltage. First, we identify a characteristic double-end streamer inception in the combined gap. Then, we propose the equivalent pulse streamer (EPS) mechanism to explain the metal particle's role. Two equivalent pulse streamers, EPS1 and EPS2, arise from the interaction between space charge and metal particle. EPS1 facilitates breakdown via the negative space charge field generated by its head. EPS2 facilitates breakdown by merging with EPS1, accelerating its propagation and enhancing the electric field at the primary streamer head. Finally, we propose the side streamer (SS) mechanism to explain the nonlinear breakdown behavior of high-pressure SF₆. The SS is identified as a new forward ionization wave that develops along the sides of the primary streamer, due to photoionization-driven negative ion accumulation. SS facilitates breakdown by merging with the primary streamer, increasing negative space charge and leading to three distinct propagation modes. Higher pressure increases the production rate of negative ions along the streamer sides, making SS more likely to form. Under overvoltage, the facilitating effect of SS diminishes as the background field $(E/N)_b$ strengthens, disappearing when $(E/N)_b$ exceeds 245 Td. This study provides new insights into the SF₆ streamer breakdown mechanisms induced by floating metal particles and offers theoretical references for further investigation on the quantitative characterization.

I. INTRODUCTION

Gas-insulated electrical equipment, such as gas-insulated switchgear (GIS) and gas-insulated transmission lines (GIL), has seen widespread use in recent years. However, SF₆ discharge faults caused by floating metal particles within the sealed chambers pose a significant risk to the safe operation of these systems [1]. This issue has emerged as a critical weakness in the insulation performance of gas-insulated equipment [2]. The electrical breakdown of SF₆ in the presence of metal particles is facilitated by two key factors: the role of floating metal particles and the nonlinear breakdown behavior of high-pressure SF₆. While previous research has examined these factors through experimental and analytical approaches, a deeper understanding of the transient microscopic characteristics remains awaiting, which motivates the research presented in this paper.

Regarding the role of floating metal particles, extensive experimental research has consistently shown that metal particles significantly reduce the gap-breakdown voltage [3–7] with linear-shaped particles with protrusions having a greater impact compared to other shapes [8, 9]. Recently, the micro-discharge theory [10–14] is commonly cited to explain the role of metal particles in facilitating breakdown. This theory is based on the short-circuit effect [15], suggesting that a particle-induced micro-discharge in the shorter gap acts as a protrusion on the electrode surface. However, the short-circuit assumptions do not fully capture the microscopic processes involved. Specifically, when a particle-induced discharge occurs, the interaction between the space charge and the metal particle redistributes the surface charge distribution on the particle [16], altering the local electric field. This, in turn, influences discharge propagation and affects breakdown behavior, but the exact role of the metal particles remains unclear.

Regarding the nonlinear breakdown behavior of SF₆, extensive experimental research has shown that its breakdown voltage varies nonlinearly with increasing gas pressure, particularly in scenarios involving electrode protrusions [17–21] and floating linear metal particles [22–24]. Some research has proposed physical mechanisms to explain this nonlinear behavior. For instance, experimental research by Gallimberti *et al.* [25] and Zhao *et al.* [26, 27] identified precursors originating from the side of the SF₆ streamer channel that promote leader formation and facilitate breakdown. Wu *et al.* [28] conducted experimental observations of a positive glow corona within the SF₆ streamer channel, whose shielding effect facilitated breakdown. Simulations by Feng *et al.* [16, 29] showed that negative ion accumulation near protrusions, secondary streamer, and fluctuations in the channel field might influence SF₆ breakdown. However, these simulations were limited to a narrow range of gas pressures. Meng *et al.* [30] simulated macroscopic characteristics of SF₆ streamers under varying pressure conditions, but the streamer channel morphology was not discussed in their paper, which is crucial for understanding the phenomena observed in high-pressure experiments.

To date, a precise understanding of these two key factors, particularly their microscopic transient behaviors, remains unclear. In this paper, we use 2D axisymmetric fluid models to investigate SF₆ streamer breakdown induced by a floating linear metal particle under negative applied voltage, with a detailed description of the model provided in Section II. In Section III, we investigate the inception of discharge in the combined gap, focusing on the characteristic double-end streamer and analyze the underlying mechanisms driving its formation. In Section IV, we propose the equivalent pulsed streamer (EPS) mechanism to illustrate the exact role of floating metal particles in facilitating breakdown. Section IV A

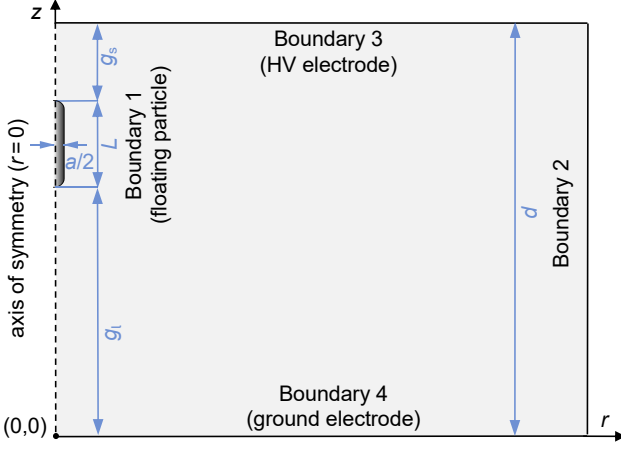


FIG. 1. Geometry of the 2D axisymmetric simulation domain and the computational boundaries.

explores the dynamics of the EPS and the mechanism driving its formation, while Section IV B examines how the EPS facilitates the breakdown process. In Section V, we propose the side streamer (SS) mechanism to illustrate the nonlinear behavior of high-pressure SF₆ and its role in facilitating breakdown. Section V A examines the dynamics of the SS, while Section V B reveals its formation mechanism and how it facilitates breakdown. Section V C presents a qualitative analysis of the pressure dependence of SS, providing insights into why it is more likely to occur at high pressure. Section V D investigates the dynamics of the SS under overvoltage conditions and its influence on the breakdown process.

II. MODEL DESCRIPTION

A. 2D Axisymmetric Geometry

The discharge electrodes are modeled as parallel plates separated by a gas gap distance $d = 5$ mm, as shown in FIG. 1. A linear metal particle, with length ($L = 1$ mm) and diameter ($a = 0.2$ mm), is positioned near the high-voltage (HV) electrode. This position reflects a typical scenario where gap breakdown occurs due to floating particles [5, 10, 13]. The gas gap between the electrodes is divided into two regions: a short gap ($g_s = 1$ mm) between the particle's top tip and the HV electrode, and a long gap ($g_l = 3$ mm) between the particle's bottom tip and the grounded electrode. The computational domain includes a sufficiently wide horizontal size to minimize edge effects. However, it is important to note that the simplified geometric structure used in this model differs from real-world scenario in terms of electrode configurations and dimensions. The following discussions clarify the the limitations arising from these differences.

Regarding electrode configuration, to accurately represent the field enhancement of particle, this paper employs an axisymmetric coordinate system. However, it cannot accurately model the coaxial cylindrical electrode structure commonly

used in GIL pipelines. As a result, the electrode configuration is further simplified to parallel plates.

Regarding dimensions, to reduce computational costs, this paper employs a reduced-sized geometry, particularly disproportionately shortening the long gap g_l compared to the real-world scenario. This reduction exaggerates the relative size of the floating particle compared to the whole space. Nonetheless, this simplification meets the research objective, which is to explore general physics during the streamer stage rather than provide precise engineering predictions.

B. Governing Equations

SF₆ streamer is considered a self-consistent, continuous conductive fluid. However, it should be acknowledged that the fluid assumption may not fully capture the kinetic characteristics [31–34] or stochastic phenomena, such as branching [35–37]. The fully kinetic model [38–40] or the hybrid model [41, 42] provide higher accuracy. Nonetheless, given the computational costs and research objectives, the fluid model remains suitable for exploring the general physics in this paper.

In the fluid model, the number density of species is obtained by solving the corresponding continuity equation:

$$\frac{\partial n_i}{\partial t} + \nabla \cdot \mathbf{\Gamma}_i = S_i \quad (1)$$

, in which n_i , $\mathbf{\Gamma}_i$, and S_i denote the number density, number flux, and source term of the i -th species, respectively.

The drift-diffusion approximation is used to determine $\mathbf{\Gamma}_i$. This approach relies on two assumptions [43]: (1) the inertia terms in the momentum equations for species are negligible, and (2) in highly collisional streamer, collisions occur on temporal scales of $\sim 10^{-12}$ s and spatial scales of $\sim 10^{-6}$ m, both of which are considerably smaller than those of electric field variations. Consequently, one can obtain:

$$\mathbf{\Gamma}_i = n_i \mathbf{u}_i = z_i \mu_i n_i \mathbf{E} - D_i \nabla n_i \quad (2)$$

, in which \mathbf{u}_i , z_i , μ_i , and D_i denote the flux velocity, charge, mobility, and diffusion coefficient of the i -th species, respectively. \mathbf{E} denotes the electric field.

The Poisson's equation is used to calculate the distribution of electric potential U :

$$\nabla^2 U = -\frac{e_0}{\epsilon_0} \sum_i z_i n_i \quad (3)$$

, in which e_0 is the elementary charge, and ϵ_0 is the vacuum permittivity. The electric field is calculated based on its defining equation:

$$\mathbf{E} = -\nabla U \quad (4)$$

The local energy approximation (LEA) can accurately capture non-local effects, particularly the dynamics of charged species near the computational boundaries [44]. Namely, the interaction between the space charge and the floating metal

particle can be ensured. Therefore, LEA framework is employed to investigate the role of floating metal particles in Section III and IV. To reduce computational costs while ensuring sufficient accuracy to meet the research objectives in Section V, the local field approximation (LFA) is employed to investigate the nonlinear breakdown behavior of high-pressure SF₆. The governing equations for these two frameworks are discussed below.

1. Local Energy Approximation (LEA)

In the context of the local energy approximation (LEA), the inclusion of the electron energy relaxation process is essential for accurately calculating electron dynamics and plasma chemistry [45, 46]. The key chemical species considered in LEA framework include e , SF₅⁺, SF₆⁻, SF₅⁻, F⁻, SF₆, SF₅, F, and SF₆^{*}. Here, SF₆^{*} represents excited electronic and vibrational levels of SF₆, treated as a single species. SF₆ serves as the background gas, and its number density is determined using the ideal gas law:

$$P = n_{\text{SF}_6} k_B T_g \quad (5)$$

, in which P denotes the gas pressure, k_B is the Boltzmann constant, and T_g denotes the gas temperature. Additionally, the number densities of other species are calculated using Eq. 1.

The plasma chemical reactions involve both electron and ion kinetics. Electron kinetics include elastic collision, ionization, attachment, excitation, and dissociation. Their reaction rates are calculated through electron collision cross-sections [47] by solving the 0D electron Boltzmann equation with the solver BOLSIG+ [48] and taken from Ref. [49]. Ion kinetics include recombination, with reaction rates taken from Ref. [50]. The source terms in Eq. 1 are determined by the net production rate, calculated based on all these reaction rates. To reduce computational costs, photoionization is approximated as a source term equivalent to 1% of the collision ionization source term. For transport coefficients in Eq. 2, electron mobility and diffusion coefficients are calculated using BOLSIG+ [48]. Ion mobilities are taken from Ref. [47], while ion diffusion coefficients are estimated using the Einstein relation, $D_{\text{ion}} = \mu_{\text{ion}} k_B T_{\text{ion}} / e$, where T_{ion} denotes the ion temperature, assumed to be equal to the gas temperature, T_g .

The electron energy conservation equation (Eq. 6) is included in the LEA framework, serving as a foundation for precise electron transport solutions, as described by Levko *et al.* [51].

$$\frac{\partial n_\epsilon}{\partial t} + \nabla \cdot \mathbf{\Gamma}_\epsilon = S_\epsilon \quad (6)$$

, in which n_ϵ denotes the electron energy density, defined as:

$$n_\epsilon = \frac{3}{2} n_e k_B T_e \quad (7)$$

, in which T_e denotes the electron temperature. $\mathbf{\Gamma}_\epsilon$ denotes the electron energy flux, defined as:

$$\mathbf{\Gamma}_\epsilon = (n_\epsilon + p_e) \mathbf{u}_e - \kappa_e \nabla T_e \quad (8)$$

, in which \mathbf{u}_e denotes the electron flux velocity, κ_e denotes the electron thermal conductivity, defined as:

$$\kappa_e = \frac{5}{2} n_e k_B D_e \quad (9)$$

p_e denotes the electron pressure, defined as:

$$p_e = n_e k_B T_e \quad (10)$$

In non-equilibrium plasmas, where $T_e \gg T_{\text{ion}}$, electrons behave as a rapidly responding fluid. In this state, the electron pressure changes slowly enough to be approximated as incompressible, resulting in $\nabla p_e = 0$. By integrating Eq. 2,8,9,10, one can obtain:

$$\mathbf{\Gamma}_\epsilon = -\frac{5}{3} \mu_e n_e \mathbf{E} - \frac{5}{3} D_e \nabla n_e \quad (11)$$

Thus, $\mathbf{\Gamma}_\epsilon$ can be determined using the previously defined μ_e and D_e .

S_ϵ is the source term for electron energy in Eq. 6, defined as:

$$S_\epsilon = -e \mathbf{\Gamma}_e \mathbf{E} - e \sum_j \Delta \epsilon_{\text{inel},j} R_j - \frac{3}{2} k_B n_e \frac{2m_e}{m_g} (T_e - T_g) \nu_{\text{el}} \quad (12)$$

, in which m_e denotes the mass of electron, m_g denotes the mass of SF₆ molecule, ν_{el} denotes the frequency of elastic collisions, $\Delta \epsilon_{\text{inel},j}$ denotes the energy change of the j -th electron-neutral inelastic collision reaction, and R_j denotes the rate of the j -th reaction. The first term in Eq. 12 denotes the electron Joule heating, while the second and third terms denote the contributions of inelastic and elastic collisions, respectively.

The critical reduced electric field $(E/N)_{\text{cr}}$ for effective ionization calculated by BOLSIG+ [48] is approximately 360 Td, which is in good agreement with the measured benchmark reported by Christophorou *et al.* [47]. In subsequent analyses utilizing LEA, $(E/N)_{\text{cr}}$ is taken to be 360 Td.

2. Local Field Approximation (LFA)

In the context of the local field approximation (LFA), the electron energy relaxation process is neglected, reducing the difficulty of numerical convergence. The LFA framework considers three species: electron, positive ion, and negative ion, with their number densities calculated using Eq. 1. The mobilities and diffusion coefficients in Eq. 2, as well as the source terms in Eq. 1 are expressed as functions of the reduced electric field E/N , consistent with those in Ref. [29]. The photoionization rate S_{ph} is calculated using Zhelezniak's model [52] and Helmholtz equations for air [53, 54] as an approximate alternative approach. The details of this alternative approach and modifications to the relevant coefficients are consistent with Ref. [29].

Notably, in the context of LFA, the critical reduced electric field $(E/N)_{\text{cr}}$ for effective ionization is 338 Td, based on ionization and attachment coefficients. It exhibits a minor deviation from the theoretical benchmark of 360 Td for pure SF₆,

primarily due to the fitting process used for these coefficients, as performed by Morrow [55]. The fitting was based on data from multiple groups [56–63], which inevitably introduced minor deviations. Nonetheless, the fitted value remains consistent with experimental trends reported by Christophorou *et al.* [47]. Consequently, this deviation does not fundamentally affect the underlying discharge mechanisms, and in subsequent analyses utilizing LFA, $(E/N)_{cr}$ is taken to be 338 Td.

C. Boundary Conditions

For the boundary conditions of the floating metal particle at Boundary 1, the current continuity equation is used to represent the effect of plasma on particle charge:

$$\frac{\partial \sigma_s}{\partial t} = \mathbf{n} \cdot \mathbf{J}_i + \mathbf{n} \cdot \mathbf{J}_e \quad (13)$$

, in which σ_s denotes the surface charge density and $\mathbf{n} \cdot \mathbf{J}_i$ and $\mathbf{n} \cdot \mathbf{J}_e$ denote the normal components of the total ion current density and the total electron current density on the particle surface, respectively. The equipotential condition is set for the metal particle surface, but time-dependent:

$$U_F \equiv \text{constant} \quad (14)$$

, in which U_F denotes the floating potential of the metal particle. Then, an integral boundary condition is set to control the overall charge Q of the metal particle:

$$\int_S \mathbf{n} \cdot \mathbf{D} dS = Q \quad (15)$$

, in which $\mathbf{n} \cdot \mathbf{D}$ denotes the normal components of the electric displacement on the particle surface. The above settings ensure that the electric field on the metal particle surface is normal to the surface and that the entire charge on the metal particle is distributed on the surface. Finally, Poisson's equation (Eq. 3), combined with the floating boundary conditions 14 and 15, ensures a self-consistent redistribution of the surface electric field and the surface charge density on the floating boundary. This redistribution reflects the electrostatic induction process of the floating metal and ensures that the metal particle is in a state of electrostatic equilibrium during every computational time step.

In addition, the kinetic Maxwellian flux condition combined with drift effect and the secondary electron emission flux, where the secondary electron emission coefficient $\gamma = 0.01$, is employed to define the boundary flux of electrons at Boundary 1, Boundary 3, and Boundary 4. The symmetric boundary condition is employed at the axis of symmetry. The homogeneous Neumann boundary condition is employed at Boundary 2. The applied voltage U_0 is employed at Boundary 3. $U \equiv 0$ is employed at Boundary 4.

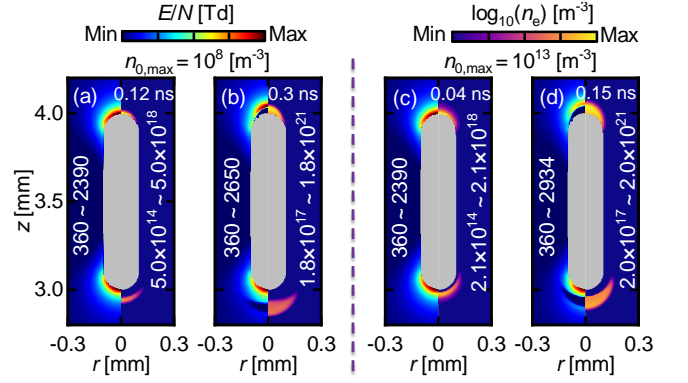


FIG. 2. Evolution of the reduced electric field E/N and Logarithmic electron density $\log_{10}(n_e)$ under different conditions: (a, b) $n_{0,\max} = 10^8 \text{ m}^{-3}$; (c, d) $n_{0,\max} = 10^{13} \text{ m}^{-3}$. $U_0 = -40 \text{ kV}$, $Q_0 = 0$, $P = 1 \text{ atm}$ and LEA is utilized with $(E/N)_{cr} = 360 \text{ Td}$ for all configurations. Labels for $(E/N)_{\min}$, $(E/N)_{\max}$, $n_{e,\min}$ and $n_{e,\max}$ are shown in each sub-figure

D. Initial Conditions

The combined gap created by a floating particle is characterized by the presence of two distinct discharge gaps, fundamentally different from a single-gap system. This structure raises two key questions regarding the initial seed " $e\text{-SF}_5^+$ " (pre-ionization) for the combined gap:

(1) Should the initial seed " $e\text{-SF}_5^+$ " be introduced in both gaps simultaneously or only in one?

(2) What should be the number density of the initial seed? The following discussions address these two questions in detail.

Firstly, the pre-ionization is set by Gaussian distributions near both the top and bottom tips of the metal particle simultaneously.:

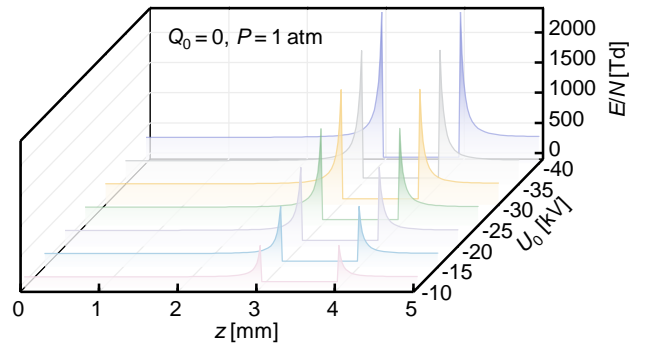


FIG. 3. Distribution of the reduced electric field E/N along the axis of symmetry at the initial moment under different U_0 .

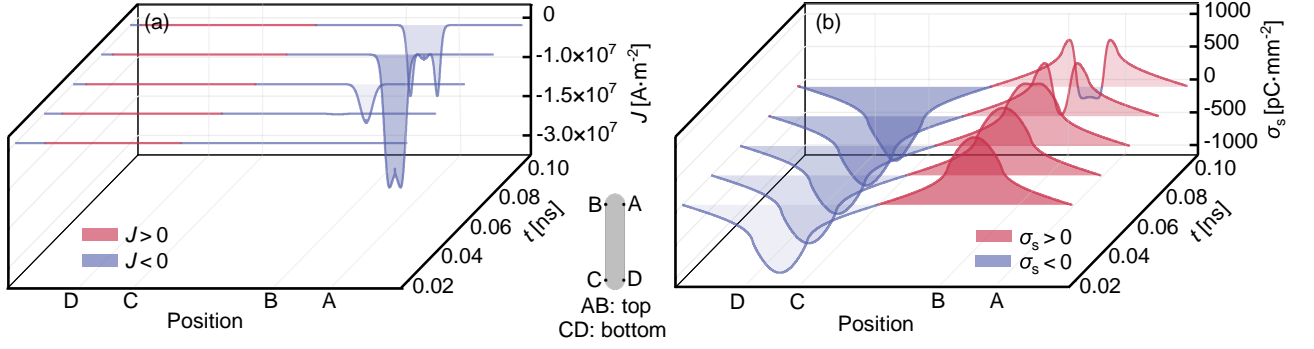


FIG. 4. Evolution of (a) current density J and (b) surface charge density σ_s along the surface of the linear metal particle, illustrating the inception of the double-end streamer

$$n_e(\text{SF}_6^+) = n_{0,\max} \left(\exp\left(-\frac{(r-0)^2}{2s_0^2} - \frac{(z-z_1)^2}{2s_0^2}\right) + \exp\left(-\frac{(r-0)^2}{2s_0^2} - \frac{(z-z_2)^2}{2s_0^2}\right) \right) \quad (16)$$

, in which $n_{0,\max}$ denotes the peak density. The parameter s_0 is set to 0.1 mm, and the Gaussian distribution centers, located at coordinates $(0, z_1)$ and $(0, z_2)$, are positioned 0.15 mm from the top and bottom tips of the particle, respectively. This dual-tip distribution is justified by the fact that, before the metal particle moves to the position necessary for combined gap breakdown, the field distortion at the two tips of the linear particle is strong enough to induce pre-ionization, as reported in Ref. [64–68].

Secondly, to accelerate the initiation and propagation of the streamer, $n_{0,\max}$ is set to 10^{13} m^{-3} . This value is artificially elevated from the typical pre-ionization level of 10^8 m^{-3} , which is observed in simulation case where $U_0 = -7 \text{ kV}$, a voltage at which the gap breakdown threshold is not satisfied. A comparison of the initial stage of streamer discharge at these two pre-ionization levels is shown in Fig. 2.

At both pre-ionization levels ($n_{0,\max}$), the initial stage of discharge exhibits a similar pattern: an electron avalanche phase (Fig. 2(a) and (c)) followed by the inception of the streamer (Fig. 2(b) and (d)). For $n_{0,\max} = 10^8 \text{ m}^{-3}$, the electron density (n_e) reaches 10^{18} m^{-3} at 0.12 ns and 10^{21} m^{-3} at 0.3 ns. At the artificially elevated level of $n_{0,\max} = 10^{13} \text{ m}^{-3}$, n_e reaches 10^{18} m^{-3} at 0.04 ns and 10^{21} m^{-3} at 0.15 ns. Consequently, one can conclude that the overall characteristics of the initial stage of discharge remain consistent, and the higher pre-ionization level further significantly accelerates the development of the discharge compared to the lower level. In addition, electron detachment is also considered a kinetic mechanism to provide initial seed electrons in SF_6 discharges for certain scenarios [69–71], and detailed comparisons remain for further investigation in the future.

The gas temperature T_g is set to 300 K, and the gas pressure P varies according to the specific studies discussed below. These two parameters are assumed to remain constant throughout the entire streamer process.

III. INCEPTION OF DOUBLE-END STREAMER

Under the conditions of $Q_0 = 0$, streamer inception induced by a floating linear metal particle occurs simultaneously at both ends, as shown in Fig. 2(b) and (d), differing notably from the behavior observed in floating dielectrics and micro-discharge theory. Mirpour and Nijdam [72] reported that for floating dielectric (TiO_2) particles under negative voltage, the positive streamer initiated first due to its lower threshold, while the negative streamer initiated only after the positive streamer had broken down. Micro-discharge theory [10–14] assumed that short-gap breakdown occurred first to establish electrical connection, allowing the floating metal particle to adopt the electrode potential, which then triggered subsequent long-gap discharge. In contrast, this paper finds that streamer inception in the long gap does not rely on short-gap breakdown, namely, double-end streamer consistently occurs in the context of floating metal particle-induced discharge. The detailed mechanisms are discussed below.

First, as shown in Fig. 3, under the initial condition $Q_0 = 0$, the electric field at both tips of the linear metal particle is approximately equal, regardless of the applied voltage. This ensures that both tips reach the effective ionization threshold $(E/N)_{\text{cr}} = 360 \text{ Td}$ simultaneously, enabling ionization at both tips, as shown in Fig. 2(a) and (c). However, ionization alone does not necessarily initiate a streamer. The electrostatic induction of the metal particle plays a critical role in the occurrence of the double-end streamer.

Further analysis of the simulation case with $U_0 = -40 \text{ kV}$, $Q_0 = 0$ and $P = 1 \text{ atm}$ illustrates this process, as shown in Fig. 4. During the early stage of ionization ($\sim 0.1 \text{ ns}$), the electron conduction current at the top tip significantly exceeds the positive ion conduction current at the bottom tip due to the higher mobility of electrons (see Fig. 4(a)). As a result, at 0.1 ns, the total charge Q on the metal particle reaches -15 pC . To maintain electrostatic equilibrium, this additional negative charge is redistributed, causing the surface charge at the bottom tip to increase from $-1035 \text{ pC} \cdot \text{mm}^{-2}$ to $-1127 \text{ pC} \cdot \text{mm}^{-2}$ (see Fig. 4(b)) in such a short period. According to Gauss's law, the surface charge density of the metal particle satisfies $\sigma_s = \epsilon E_s$. As a result, during the initial stage of ionization ($\sim 0.1 \text{ ns}$), the electric field at the bottom tip, already exceeding $(E/N)_{\text{cr}}$, is

further increased by ~ 200 Td. This enhancement promotes the inception of the double-end streamer, as shown in Fig. 2.

IV. ROLE OF METAL PARTICLE: EQUIVALENT PULSED STREAMER (EPS) MECHANISM

The breakdown mechanism in the combined gas gap induced by floating metal particles primarily highlights how these particles facilitate long-gap (g_1) breakdown. This section investigates the physical processes through which floating metal particles contribute to long-gap breakdown. From a phenomenological perspective, floating metal particles play a pivotal role, which we refer to in this paper as the "equivalent pulsed streamer (EPS)" mechanism. As shown in Fig. 5(i), the primary streamer in the long-gap breakdown is followed by two independent streamers, labeled EPS1 and EPS2. This pattern closely resembles the multiple streamer events commonly observed under pulsed voltage conditions [73–76].

Notably, It is essential to distinguish the subsequent streamers discussed here from those arising solely from the accumulation of negative ions in SF₆ gas, as described in Ref. [16]. The primary difference lies in the characteristics of the electric field within the streamer channel. For the secondary streamer described in Ref. [16], the channel field is quickly shielded below the critical value $(E/N)_{\text{cr}}$. In contrast, for the EPS mechanism discussed in this paper, the channel field remains above $(E/N)_{\text{cr}}$ for a period after the streamer is initiated, as shown in Fig. 5(b) and (i).

This difference can be attributed to the negative surface charge at the bottom tip of the floating metal particle, which primarily drives the multiple streamers in the EPS mechanism, as shown in Fig. 5(g). Because the metal particle remains in electrostatic equilibrium, Gauss's law ensures that the condition $\sigma_s = \epsilon E_s$ is consistently satisfied on its surface. This equilibrium causes the surface electric field at the particle's bottom tip to intensify, similar to the effect of the rising edge of a pulsed voltage. As a result, the linear floating metal particle behaves as an equivalent pulsed source, inducing subsequent streamers referred to as EPS. The detailed physical mechanisms underlying how the metal particle induces EPS are further discussed in Section IV A.

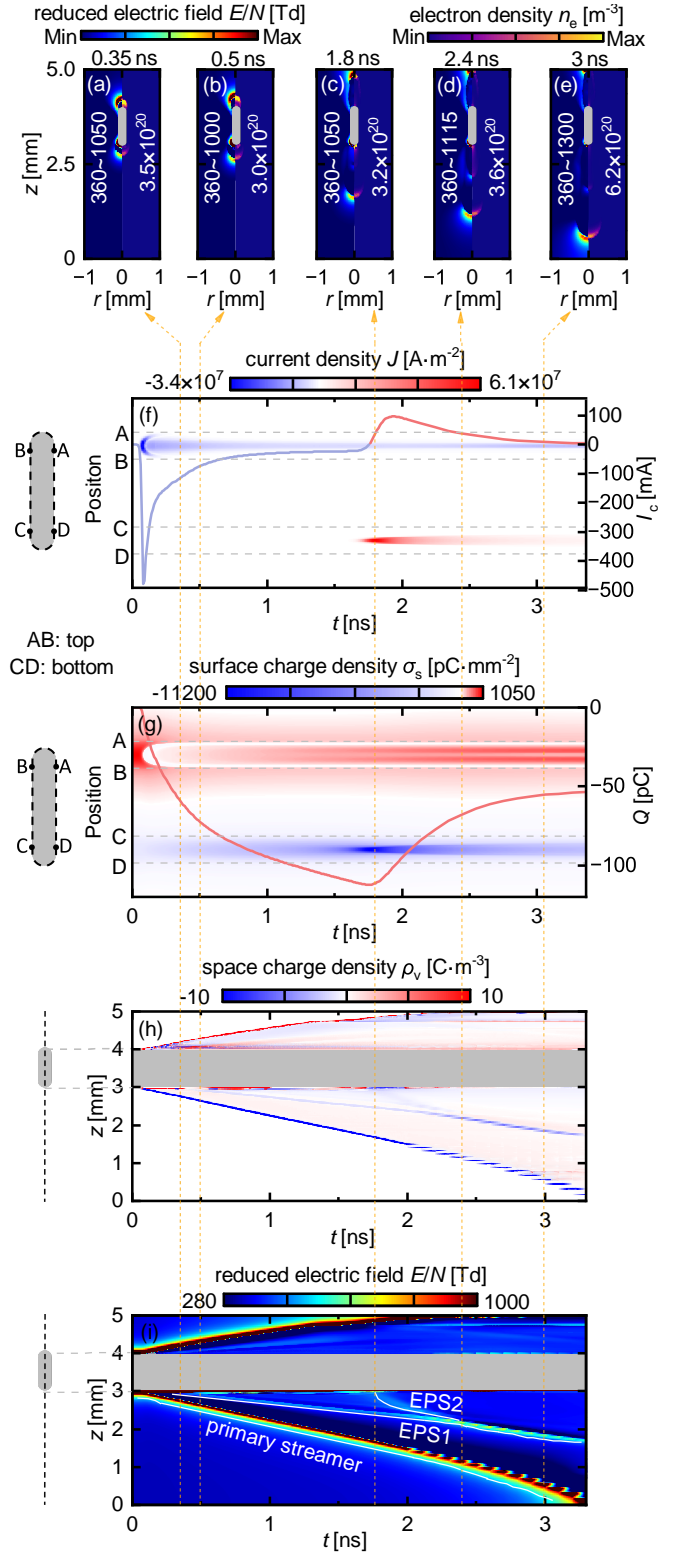


FIG. 5. (a-e) Evolution of the reduced electric field E/N and electron density n_e . Labels for $(E/N)_{\text{min}}$, $(E/N)_{\text{max}}$ and $n_{e,\text{max}}$ are shown in each sub-figure, where $n_{e,\text{min}}$ is fixed at 0. (f) Spatiotemporal evolution of current density J along the surface of metal particle and the temporal evolution of the total conduction current I_c . (g) Spatiotemporal evolution of surface charge density σ_s along the surface of metal particle and temporal evolution of the total charge Q . (h) Spatiotemporal evolution of space charge density ρ_v along the axis of symmetry. (i) Spatiotemporal evolution of reduced electric field E/N along the axis of symmetry. The white lines show the position of the streamer head. $U_0 = -40\text{kV}$, $Q_0 = 0$, $P = 1\text{ atm}$ and LEA is utilized with $(E/N)_{\text{cr}} = 360\text{ Td}$.

A. Dynamics and Mechanism of Equivalent Pulsed Streamer (EPS)

At 0.5 ns, the first equivalent pulsed streamer (EPS1) initiates, as shown in Fig. 5(a) and (b). This process is driven by two critical aspects: the electron charging effect at the particle's top tip and the electrostatic induction of the entire metal particle, both of which are indispensable. During the 0–0.5 ns interval, under the influence of the negative applied voltage, electrons migrate rapidly toward the particle's top tip, generating a negative conduction current at this location. In contrast, ions migrate more slowly, and no significant conduction current is observed at the particle's bottom tip. As a result, the total conduction current I_c acting on the metal particle peaks at -500 mA (see Fig. 5(f)), highlighting the dominant role of electron charging during this phase. This charging process causes a steady accumulation of negative charge Q on the metal particle, exceeding -73 pC, as shown in Fig. 5(g).

Notably, although the negative charge primarily accumulates at the particle's top tip due to electron conduction, the negative surface charge at the bottom tip also increases significantly, rising from -1034 pC \cdot mm $^{-2}$ at 0 ns to -2076 pC \cdot mm $^{-2}$ at 0.5 ns (see Fig. 5(g)). This behavior is fundamentally governed by the electrostatic induction of the floating metal particle, namely, to maintain electrostatic equilibrium, the surface charge on the particle undergoes a self-consistent redistribution. As a result, the negative surface charge gradually increases at the particle's bottom tip. The space electric field induced by this negative surface charge, aligned with the applied electric field, enhances the local electric field near the particle's bottom tip, thereby enhancing ionization in the sheath in this region, as shown in Fig. 5(a).

The positive feedback mechanism described in Ref. [16] further promotes the attachment of sheath electrons near the bottom tip, resulting in the formation of a negative ion region and an increase in negative space charge within this region (see Fig. 5(h)). The combined effect of the negative space charge in the negative ion region and the negative surface charge at the particle's bottom tip intensifies the local electric field. After 0.35 ns, the reduced field outside the sheath exceeds the critical value $(E/N)_{cr}$. By 0.5 ns, EPS1 initiates from this position and propagates forward, maintaining the same polarity as the primary streamer, with both being negative streamers (see Fig. 5(h)).

At 1.8 ns, the second equivalent pulsed streamer (EPS2) initiates, as shown in Fig. 5(c) and (d). This phenomenon is driven by two aspects: the positive ion charging effect at the particle's bottom tip and the electrostatic induction of the entire metal particle. Starting at 1.72 ns, ion migration becomes significant. The particle's bottom tip sustains a positive conduction current (mainly from positive ions), while the top tip sustains a negative conduction current (dominated by electrons, which contribute six times more than negative ions). After 1.8 ns, the positive conduction current at the bottom tip surpasses the negative conduction current at the top tip, causing the total conduction current I_c to exceed 65 mA (see Fig. 5(f)), and leading to a decrease in the net negative charge Q on the particle (see Fig. 5(g)).

Notably, although the positive charge primarily accumulates at the bottom tip due to positive ion conduction, electrostatic induction redistributes some of this positive charge to the top tip, increasing the positive surface charge there. Meanwhile, the bottom tip induces more negative surface charge, reaching a maximum density of -11200 pC \cdot mm $^{-2}$. The negative surface charge at the bottom tip, together with the negative space charge near the particle's bottom tip and the positive surface charge at the top tip, establish a self-consistent electrostatic equilibrium. At this stage, the induced negative surface charge at the bottom tip significantly enhances the local electric field near the bottom tip. The combined effects of the negative space charge in the negative ion region and the negative surface charge ultimately induce the second equivalent pulsed streamer (EPS2), which remains the same negative polarity as the previous streamers, as shown in Fig. 5(h).

B. Equivalent Pulsed Streamer (EPS) Facilitation on Breakdown

The propagation speed of the streamer is qualitatively estimated from the slope of the streamer head trajectory line in Fig. 5(i), namely, a steeper slope (greater displacement in the z -direction per unit time) indicates faster propagation.

The facilitating effect of EPS1 on long-gap breakdown is primarily driven by the space charge field generated by the negative space charge at its head. As shown in Fig. 5(h), EPS1, functioning as a negative streamer, generates the space charge field that is aligned with the applied electric field. This alignment enhances the local field at the primary streamer head, maintaining the reduced electric field at ~ 1000 Td, as shown in Fig. 5(i). In comparison to the single negative streamer scenario reported in Ref. [77], where the electric field at the streamer head typically decreases by ~ 30 Td and the propagation speed is drops by 43%, the presence of EPS1 in this paper mitigates the decline of the electric field at primary streamer head. As a result, under the influence of EPS1, the propagation speed of the primary streamer remains nearly constant, as shown in Fig. 5(i), instead of slowing down. Thus, one can conclude that EPS1 significantly enhances the propagation of the primary streamer, thereby facilitating the breakdown of the long gap.

The facilitating effect of EPS2 on long-gap breakdown arises from its merging with EPS1. As shown in Fig. 5(h), at 2.4 ns, EPS2 merges with EPS1, causing an increase in the space charge density ρ_v at the head of EPS1 from -1.5 C \cdot m $^{-3}$ at 1.8 ns to -5.3 C \cdot m $^{-3}$ at 2.4 ns. This increase in space charge strengthens the electric field at the head of EPS1, raising it from 480 Td at 1.8 ns to 708 Td at 2.4 ns, as shown in Fig. 5(i). After the merging, the propagation speed of EPS1 is significantly accelerated. The rise in negative space charge at the head of EPS1 also enhances the reduced field at the primary streamer head, increasing it from 1050 Td at 1.8 ns to 1115 Td at 2.4 ns, as shown in Fig. 5(c) and (d). Consequently, after 2.4 ns, the propagation speed of the primary streamer noticeably accelerates, as shown in Fig. 5(i). Thus, one can conclude that EPS2 significantly enhances the

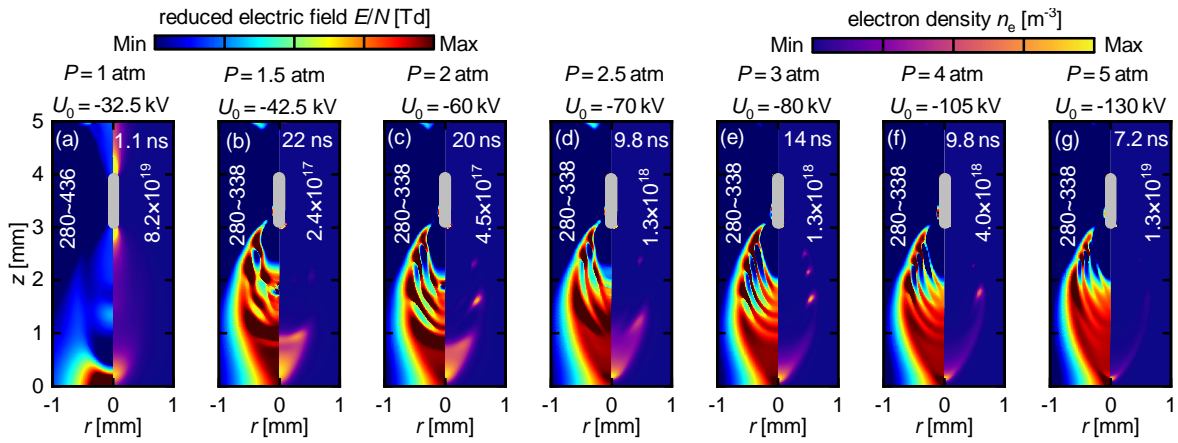


FIG. 6. Evolution of the reduced electric field E/N and electron density n_e under different conditions: (a) $P = 1$ atm, $U_0 = -32.5$ kV; (b) $P = 1.5$ atm, $U_0 = -42.5$ kV; (c) $P = 2$ atm, $U_0 = -60$ kV; (d) $P = 2.5$ atm, $U_0 = -70$ kV; (e) $P = 3$ atm, $U_0 = -80$ kV; (f) $P = 4$ atm, $U_0 = -105$ kV; (g) $P = 5$ atm, $U_0 = -130$ kV. $Q_0 = 0$ and LFA is utilized with $(E/N)_{cr} = 338$ Td for all configurations. Labels for $(E/N)_{min}$, $(E/N)_{max}$ and $n_{e,max}$ are shown in each sub-figure, where $n_{e,min}$ is fixed at 0.

propagation of the primary streamer, ultimately facilitating the breakdown of the long gap.

V. NONLINEAR BEHAVIOR OF HIGH-PRESSURE SF₆: SIDE STREAMER (SS) MECHANISM

In practical applications, gas-insulated electrical equipment typically operates at pressures above atmospheric levels. Consequently, particle-induced SF₆ discharge in real scenarios inevitably occurs under high-pressure conditions. Therefore, we investigate the effect of gas pressure on SF₆ streamer propagation in the context of particle-structure electrodes. The use of particle-structure electrodes is justified by two main considerations. First, it aligns with the subject of this paper, ensuring consistency in the investigative framework. Second, analyzing the effects of gas pressure within the particle-structure framework is physically valid. Specifically, gas pressure does not fundamentally alter the interaction between the metal particle and the space charge, as this interaction is governed by the intrinsic electrostatic induction properties of the metal. This decoupling of gas pressure effects from the behavior of the metal particle confirms that the particle-structure electrode is adequate for addressing the research objectives.

As outlined in Section I, the nonlinear breakdown behavior of high-pressure SF₆ is closely linked to the distinctive streamer morphologies under high-pressure conditions. In this section, we investigate the dynamics of high-pressure SF₆ streamer morphologies in the context of LFA framework. It should be acknowledged that, although the LFA framework cannot fully capture the interaction between the space charge and the metal particle, it is effective for modeling solely the dynamics of streamer propagation in the combined gap, as reported in Ref. [78–81]. This makes LFA an appropriate framework for the objectives of this section, and it also offers the advantage of significantly reducing computational costs. For simplicity, in the following discussions, the term

"streamer" will exclusively refer to those occurring in the long gap, excluding those in the short gap.

A. Dynamics of Side Streamer (SS)

1. Side Streamer (SS) Phenomenon

The simulation cases are conducted at pressure levels of 1 atm, 1.5 atm, 2 atm, 2.5 atm, 3 atm, 4 atm, and 5 atm. In all the cases below, the initial charge $Q_0 = 0$. The applied voltage U_0 is set at a near-critical voltage, exceeding the breakdown threshold. This voltage allows for an observation qualitatively consistent with critical behavior while also highlighting the characteristics of streamer propagation. The results of SF₆ streamer propagation at near-critical voltages under varying pressures are shown in Fig. 6. For clarity, the term "primary streamer" refers to the discharge at the forefront, propagating along the axis.

At 1 atm, as shown in Fig. 6(a), the streamer behavior is consistent with the findings in Section IV, exhibiting multiple streamer characteristics. In contrast, at pressures of 1.5 atm or higher, as shown in Fig. 6(b-g), the streamer develops a distinct coherent structure, markedly different from the patterns observed at atmospheric pressure. This coherent structure forms along the side of the primary streamer channel and is characterized by a localized region of field enhancement where $E/N > (E/N)_{cr}$. Within this enhanced field region, localized areas of high electron density n_e , exceeding 10^{17} m^{-3} , indicate the occurrence of intense ionization. To determine whether this coherent structure constitutes the formation of a new streamer, it is necessary to determine if the field enhancement regions within it shift spatially, which could signal the propagation of an ionization wave.

For detailed analysis, the simulation case with $P = 4$ atm and $U_0 = -105$ kV is examined, as shown in Fig. 7, which illustrates the complete streamer propagation process. A co-

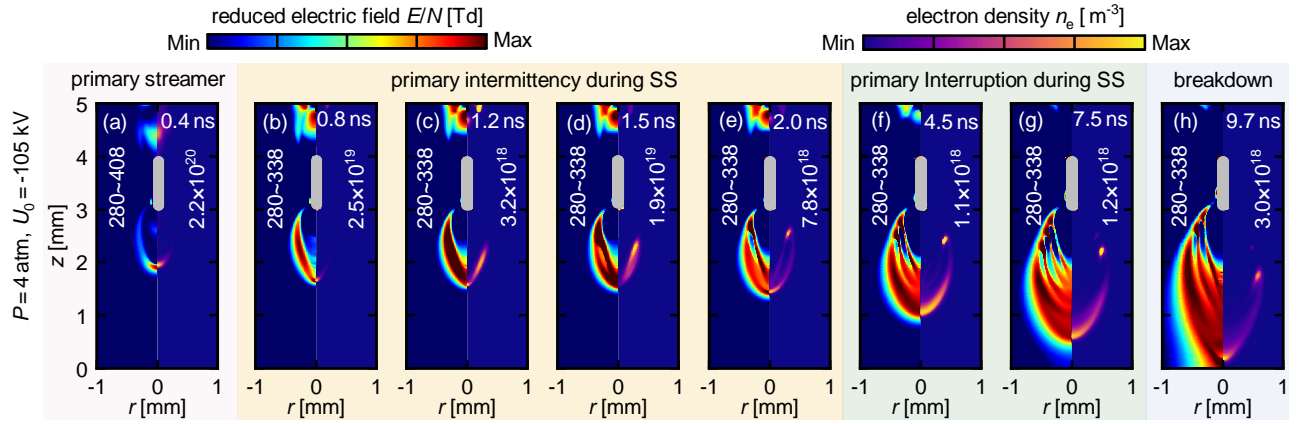


FIG. 7. Evolution of the reduced electric field E/N and electron density n_e under near-critical voltage $U_0 = -105$ kV and at pressure of 4 atm. $Q_0 = 0$ and LFA is utilized with $(E/N)_{cr} = 338$ Td for all configurations. Labels for $(E/N)_{min}$, $(E/N)_{max}$ and $n_{e,max}$ are shown in each sub-figure, where $n_{e,min}$ is fixed at 0.

herent structure is observed forming along the side of the primary streamer and propagates forward as an ionization wave in the same direction, as shown in Fig. 7(b-e). This coherent structure essentially behaves as a new streamer with the same polarity as the primary one. In this paper, we refer to this new type of streamer as "side streamer (SS)" to emphasize its formation and propagation alongside the primary streamer. Interestingly, multiple SS can emerge during a single discharge event, as shown in Fig. 7(f) and (g). Each SS follows a fundamentally similar pattern, forming sequentially along the side of its predecessor. This process results in a characteristic "layer-by-layer nesting" spatial arrangement.

2. Impact of Side Streamer (SS) on Primary Streamer

Another important aspect to investigate is the impact of the SS phenomenon on the primary streamer. In the presence of SS, the primary streamer exhibits two distinct propagation modes. The first mode, referred to as "primary intermittency", is shown in Fig. 7(b-e). In this mode, during SS propagation, the reduced field E/N at the primary streamer head gradually decreases to below $(E/N)_{cr}$, accompanied by a reduction in electron density n_e by approximately one order of magnitude. This temporarily halts the forward propagation of the primary streamer, as shown in Fig. 7(b) and (c). However, when the SS reaches the primary streamer head, the reduced field E/N recovers to above the $(E/N)_{cr}$, re-establishing intense ionization. This recovery increases the electron density n_e at the streamer head from $2 \times 10^{18} \text{ m}^{-3}$ to $7.8 \times 10^{18} \text{ m}^{-3}$, as shown in Fig. 7(d) and (e). These characteristics demonstrate a transition in the primary streamer from a temporary pause to resumed axial propagation, defining the primary intermittency mode.

After propagating a certain distance, the primary streamer transitions to another mode, referred to as "primary interruption". In this mode, even after the SS merges with the primary streamer, the streamer head does not fully recover its strong reduced field, remaining at $E/N < (E/N)_{cr}$, as shown

in Fig. 7(f) and (g). This indicates that the primary streamer remains in an interrupted state, with insufficient ionization level at its head. Surprisingly, an unusual phenomenon is observed: despite this interruption, the region ahead of the primary streamer—characterized by an enhanced but sub-critical reduced field $E/N < (E/N)_{cr}$ —continues to propagate forward. In this forward region, the electron density remains around $n_e \approx 1 \times 10^{18} \text{ m}^{-3}$. Although this density is lower than during fully active streamer propagation, it reflects the continuous generation of new electrons through ionization.

These observations indicate that under high-pressure conditions, SF_6 streamers propagation is strongly influenced by the SS phenomenon. The presence of SS leads the primary streamer to exhibit distinct propagation modes. The underlying physical mechanisms driving the SS phenomenon and its influence on the primary streamer are analyzed in the following sections.

B. Mechanism of Side Streamer (SS) and Its Facilitation on Breakdown

To investigate the physical mechanisms underlying the SS phenomenon, the simulation case with $P = 4$ atm and $U_0 = -105$ kV is analyzed in detail in this section. Given the uniform behavior of each SS within the layer-by-layer nesting pattern, the first SS event is selected as a representative case. Key physical parameters, including the photoionization rate (S_{ph}), effective ionization rate (S_{eff}), space charge density (ρ_v), and reduced electric field (E/N), are systematically examined. For clarity and precision, the SS phenomenon is divided into four distinct stages: pre-initiation, initiation, propagation, and merging. Each stage is individually analyzed to provide a comprehensive understanding of the underlying mechanisms.

The pre-initiation stage is analyzed at 0.75 ns and 0.81 ns to illustrate the preparatory processes leading to SS formation. As shown in Fig. 8(a1), (a2), (b1) and (b2), on the side of the primary streamer, the effective ionization rate ($S_{eff} < 0$)

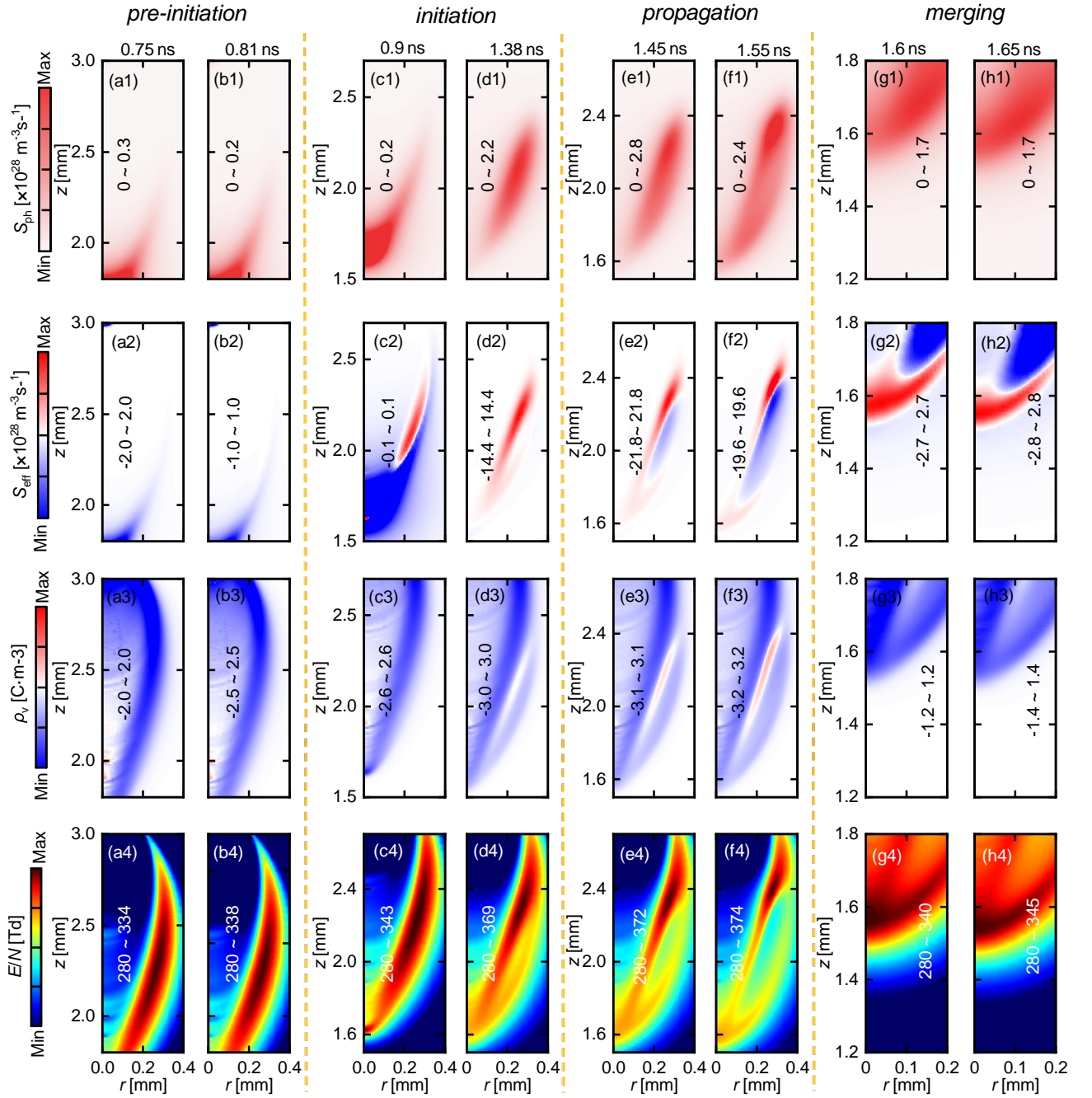


FIG. 8. Evolution of the (a1-h1) photoionization rate S_{ph} , (a2-h2) effective ionization rate S_{eff} , (a3-h3) space charge density ρ_v and (a4-h4) reduced electric field E/N , illustrating SS mechanism under near-critical voltage $U_0 = -105$ kV and at pressure of 4 atm. $Q_0 = 0$ and LFA is utilized with $(E/N)_{cr} = 338$ Td for all configurations.

and photoionization rate ($S_{ph} > 0$) exhibit opposite behaviors due to their different physical definitions. Specifically, S_{ph} is positively correlated with $\alpha n_e \mu_e E$, in which α denotes the ionization coefficient, while $S_{eff} = (\alpha - \eta) n_e \mu_e E$, in which η denotes the attachment coefficient. Thus, S_{ph} is solely related to collision ionization, while S_{eff} reflects the net effect of ionization and attachment during the electron collision process. This distinction results in continuous generation of seed electrons on the side of channel via photoionization, even as they

are rapidly attached, leading to the accumulation of negative ions there. As a result, the negative space charge on the side increases, as shown in Fig. 8(a3) and (b3). The space charge field generated aligns with the applied negative-polarity electric field, enhancing the local field on the side from 334 Td to 338 Td ($(E/N)_{cr}$), as shown in Fig. 8(a4) and (b4).

The initiation stage is analyzed at 0.9 ns and 1.38 ns to illustrate the onset of SS formation. At 0.9 ns, the continued accumulation of negative ions from the pre-initiation stage

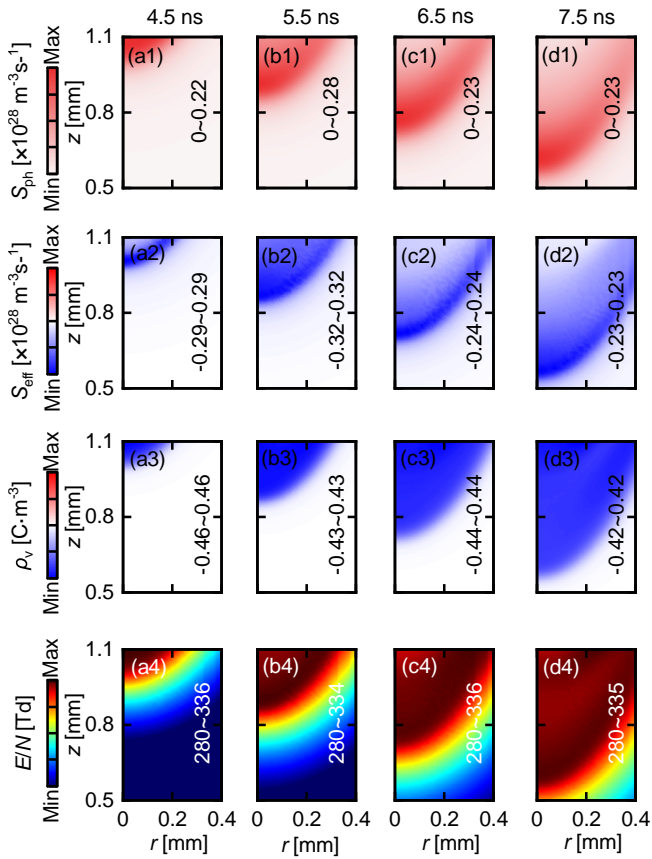


FIG. 9. Evolution of the (a1-d1) photoionization rate S_{ph} , (a2-d2) effective ionization rate S_{eff} , (a3-d3) space charge density ρ_v and (a4-d4) reduced electric field E/N , illustrating primary interruption mode under near-critical voltage $U_0 = -105$ kV and at pressure of 4 atm. $Q_0 = 0$ and LFA is utilized with $(E/N)_{cr} = 338$ Td for all configurations.

causes the local field on the side to exceed $(E/N)_{cr}$, as shown in Fig. 8(c4). This marks the beginning of electron generation through electron collision process, although it remains weaker than photoionization ($S_{eff} < S_{ph}$), as shown in Fig. 8(c1) and (c2). At 1.38 ns, a spatial shift in the space charge distribution signals the emergence of a new ionization wave—SS—with the same negative polarity as the primary streamer, as shown in Fig. 8(d3). During this time, $S_{eff} \approx 6.5 \cdot S_{ph}$, as shown in Fig. 8(d1) and (d2), indicating a significant intensification of electron collision process. This intensification allows electron collision process to surpass photoionization as the dominant electron generation mechanism, thereby facilitating the formation of the SS.

The propagation stage is analyzed at 1.45 ns and 1.55 ns to illustrate the behavior of SS as an ionization wave. During this stage, the effective ionization rate (S_{eff}) significantly exceeds the photoionization rate (S_{ph}), with $S_{eff} \approx 8 \cdot S_{ph}$. This indicates that electron collision process dominates the electron generation. As the SS propagates forward, the negative space charge at its head generates a shielding effect that weakens the electric field in the region behind it, reducing the reduced field below $(E/N)_{cr}$, as shown in Fig. 8(e4) and (f4). In

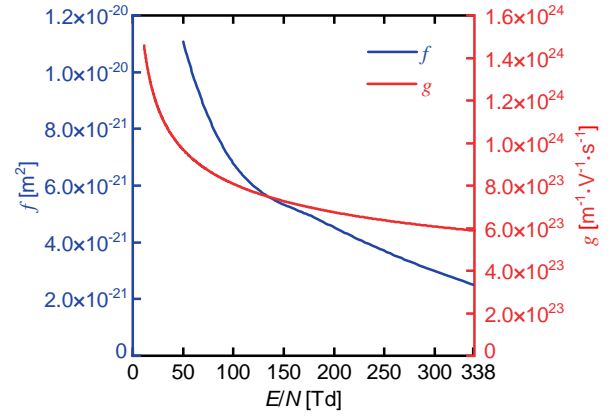


FIG. 10. Functions f and g as defined in the analysis.

this low-field region, the electron attachment surpasses electron generation, resulting in $S_{eff} < 0$. This process leads to the formation of a well-defined streamer channel of SS.

The merging stage is analyzed at 1.6 ns and 1.65 ns to illustrate the process of the SS merging with the primary streamer and its facilitation on breakdown. As the SS propagates forward, it gradually moves toward the axis where the primary streamer is located. This movement is driven by the negative space charge generated by the primary streamer, as shown in Fig. 8(g3) and (h3). The negative space charge enhances the local field near the axis, as shown in Fig. 8(g4) and (h4), which in turn intensifies ionization near the axis, as shown in Fig. 8(g2) and (h2). As a result, the SS develops consistently toward the axis until it merges with the primary streamer. Following the merging, the SS disappears, and the negative space charge on the axis increases from $-1.2 \text{ C} \cdot \text{m}^{-3}$ to $-1.4 \text{ C} \cdot \text{m}^{-3}$, as shown in Fig. 8(g3) and (h3). This increase in space charge restores the local electric field at the primary streamer head to 345 Td, exceeding the critical value $(E/N)_{cr}$. As a result, the primary streamer resumes its propagation along the axis, forming the primary intermittency mode as described in Section V A 2.

After the merging stage of the SS, the primary streamer can exhibit an unusual phenomenon: the primary interruption mode, as shown in Fig. 7(f) and (g) and described in Section V A 2. The primary physical factor driving its propagation is photoionization, with the detailed mechanism illustrated in Fig. 9. The SS merging restores the primary streamer head to a near-critical field strength, i.e., near but below the critical value $(E/N)_{cr}$ (see Fig. 9(a4)), thus, photoionization remains consistently active (see Fig. 9(a1-d1)) and the effective ionization rate S_{eff} remains negative (see Fig. 9(a2-d2)). As a result, the seed electrons at the front generated by photoionization rapidly attach to form negative ions at the front, gradually expanding the negative space charge region, as shown in Fig. 9(c3-d3). This negative space charge enhances the local field at the front, enabling the near-critical enhanced field region to expand forward spatially, even though the field remains below $(E/N)_{cr}$, as shown in Fig. 9(c4-d4). In summary, the primary interruption mode is based on the SS merging, which restores the primary streamer head to a near-critical

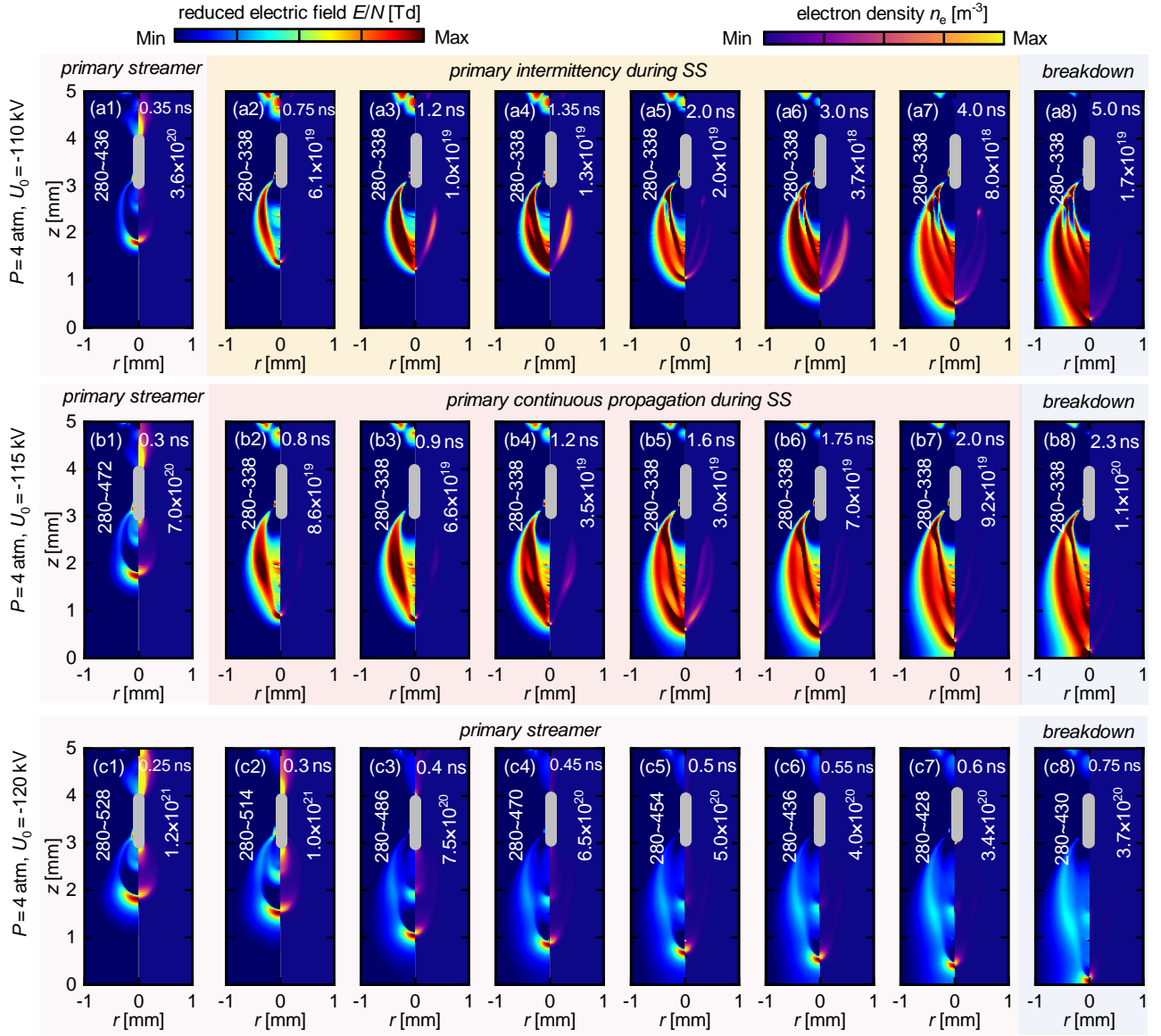


FIG. 11. Evolution of the reduced electric field E/N and electron density n_e , illustrating the SS phenomenon under different overvoltage levels: (a1-a8) $U_0 = -110$ kV; (b1-b8) $U_0 = -115$ kV; (c1-c8) $U_0 = -120$ kV. $P = 4$ atm. $Q_0 = 0$ and LFA is utilized with $(E/N)_{cr} = 338$ Td for all configurations. Labels for $(E/N)_{min}$, $(E/N)_{max}$, and $n_{e,max}$ are shown in each sub-figure, where $n_{e,min}$ is fixed at 0.

field strength, maintaining a relatively high level of photoionization. On this basis, the collaboration of photoionization and attachment drives the forward expansion of the negative space charge region at the streamer head, leading to its propagation. As it expands further and approaches the vicinity of the grounded electrode, the field strength at the head is enhanced once again, exceeding $(E/N)_{cr}$, as shown in Fig. 7(h). This enables the primary streamer to continue propagating, ultimately resulting in breakdown.

C. Pressure Dependence of Side Streamer (SS): Qualitative Analysis

The reduced electric field E/N at the SS initiation position remains below than the critical value $(E/N)_{cr}$ during the pre-initiation stage, as shown in Fig. 8. Therefore, the subsequent analysis is confined to the range $E/N < (E/N)_{cr}$. Since this section focuses on the dependence of gas pressure, the applied electric field E_0 is considered the same across different pressure conditions.

As discussed in Section VB, the primary species driving SS initiation is the negative ion, and its production rate S_n is defined as $S_n = \eta \mu_e n_e E$. Based on the expressions for η and μ_e in Ref. [29], one can obtain $\eta = f(E/N) \cdot N$ and $\mu_e = \frac{g(E/N)}{N}$.

Thus, S_n can be expressed as $S_n = f(E/N)g(E/N)n_eE$. It is important to note that during the early pre-initiation stage of SS, the initiation position retains the properties of the SF₆ streamer channel. According to Ref. [16, 29], the electric field E within the SF₆ streamer channel consistently recovers to a level roughly equivalent to the applied electric field E_0 . Moreover, the electron density n_e at the SS initiation position, approximately $n_e \approx 10^{17} \text{ m}^{-3}$, is supplied by photoionization and varies little under different pressure conditions. Consequently, the initial value of S_n under different pressures, which determines the initiation of SS, is primarily determined by $f(E/N)$ and $g(E/N)$.

From a qualitative perspective, as $P \uparrow, N \uparrow$; since $E = E_0$ remains constant, $E/N \downarrow$. Both $f(E/N)$ and $g(E/N)$ are monotonically decreasing functions of E/N , as shown in Fig. 10, thus $f(E/N)g(E/N) \uparrow$. Given $S_n \propto f(E/N)g(E/N)$, it follows that $S_n \uparrow$. Hence, one can conclude that higher pressures facilitate negative ion generation, making SS initiation more likely, as shown in Fig. 6.

D. Dynamics of Side Streamer (SS) under Overvoltage

In practical gas-insulated equipment, overvoltage conditions are inevitable. Therefore, it is essential to examine whether the SS mechanism continues to influence SF₆ high-pressure streamer breakdown under overvoltage conditions. This section investigates whether the role of the SS mechanism in the development of primary streamer remains consistent at overvoltage levels compared to its behavior at near-critical voltage. To address this, simulation cases are conducted at a representative gas pressure of 4 atm. The applied voltages U_0 are varied at -110 kV , -115 kV , and -120 kV , respectively. The corresponding results are shown in Fig. 11.

When the applied voltage is set to $U_0 = -110 \text{ kV}$, corresponding to a background reduced field $(E/N)_b \approx 225 \text{ Td}$, the SS phenomenon remains observable and the primary streamer propagates in the same primary intermittency mode as observed at near-critical voltage. This indicates that at this overvoltage level, the elevated $(E/N)_b$ enables the local field at the head of the primary streamer to recover above $(E/N)_{cr}$ after merging with the SS, as shown in Fig. 11(a5-a7). However, despite the elevated $(E/N)_b$ compared to the near-critical condition, the primary streamer still experiences temporary pause before merging with the SS, as shown in Fig. 11(a2-a4). This indicates that at this overvoltage level, the elevated $(E/N)_b$ alone is insufficient to sustain continuous propagation. Instead, the additional negative space charge contributed by the merging SS remains the key factor that enabling the primary streamer to resume propagation.

When the applied voltage is increased to $U_0 = -115 \text{ kV}$, corresponding to a background reduced field $(E/N)_b \approx 235 \text{ Td}$, the SS phenomenon remains observable; however, the primary streamer exhibits a new propagation mode, referred to as "primary continuous propagation", distinct from the primary intermittency or primary interruption modes discussed in Section V A 2. As shown in Fig. 11(b1-b8), the local field at the primary streamer head consistently exceeds

$(E/N)_{cr}$ throughout propagation, and the electron density n_e at the head remains greater than 10^{19} m^{-3} . This behavior results from the elevated $(E/N)_b$, which enables a high ionization level, allowing the primary streamer to sustain independent propagation without relying on additional negative space charge from SS merging. Nevertheless, the SS phenomenon continues to play a supportive role. During merging, the head field is further enhanced, increasing from 357 Td to 368 Td , facilitating faster propagation.

When the applied voltage is further increased to $U_0 = -120 \text{ kV}$, corresponding to $(E/N)_b \approx 245 \text{ Td}$, the primary streamer crosses the gap in just 0.75 ns , as shown in Fig. 11(c8)). The rapid propagation significantly reduces the opportunity for the SS mechanism to develop, as shown in Fig. 11(c1-c8). This result indicates that under extreme overvoltage conditions, characterized by a substantially elevated $(E/N)_b$, the SS mechanism plays a negligible role in high-pressure SF₆ streamer breakdown process.

VI. CONCLUSIONS

In this paper, we simulate and analyze the SF₆ streamer breakdown induced by a floating linear metal particle under negative applied voltage. Our key findings are summarized as follows:

(1) Initial discharge stage: we investigate the inception of the discharge within the combined gap under the condition $Q_0 = 0$. The discharge inception manifests as a double-end streamer, without a clear sequential initiation between the long and short gaps. This behavior contrasts with floating dielectric (TiO₂) discharge or micro-discharge theory, where discharge typically initiates in a sequence. Simultaneous ionization at both tips of the metal particle causes electrons from the short gap to conduct to particle for charging. Subsequently, the redistribution of negative charge due to the particle's electrostatic induction enhances the electric field near the long gap, causing both ends to exceed the streamer threshold.

(2) Two mechanisms facilitating breakdown: we examine two key factors that facilitate breakdown: the role of floating metal particles and the nonlinear breakdown behavior of high-pressure SF₆. Based on their microscopic transient behaviors, we propose the equivalent pulse streamer (EPS) mechanism and the side streamer (SS) mechanism, respectively. An in-depth and thorough analysis of their dynamics, formation mechanism, and breakdown-facilitating mechanism is conducted. The dominant physical parameters and properties driving them are also identified.

(3) Role of floating metal particles: we find that the negative surface charge and surface electric field at the particle's bottom tip continuously increase, similar to the effect of the rising edge of a pulse voltage. This induces two equivalent pulse streamers (EPS1 and EPS2) in the long gap, with the same polarity as the primary streamer. EPS1 is dominated by the charging effect of electron conduction from the short gap and the electrostatic induction of the metal particle; EPS1 facilitates breakdown by generating a negative space charge field,

which enhances the electric field at the primary streamer head. EPS2 is dominated by the charging effect of positive ions from the long gap and the electrostatic induction of the metal; EPS2 facilitates breakdown by merging with EPS1, which increases the negative space charge at the EPS1 head. This not only accelerates the propagation of EPS1 but also further enhances the electric field at the primary streamer head.

(4) Nonlinear behavior of high-pressure SF₆: we find that the side streamer (SS), a new forward ionization wave, forms along the sides of the primary streamer. The formation of SS is dominated by photoionization, with photoelectrons attaching to the sides and forming negative ions, leading to the enhancement of the side field. SS facilitates breakdown by merging with the primary streamer, thereby increasing the negative space charge at the streamer head and enhancing the head electric field. After merging, if the head field exceeds $(E/N)_{cr}$, the primary streamer exhibits a primary intermittency mode; if the head field remains near but below $(E/N)_{cr}$, the collaboration of photoionization ($S_{ph} > 0$) and effective ionization $S_{eff} < 0$ drives the forward expansion of the negative space charge region at the streamer head, leading to a primary interruption mode.

(5) Pressure dependence of side streamer (SS): qualitative analysis indicates that higher pressure results in higher negative ion production rate S_n at the SS initiation position, making SS more likely to form under high-pressure conditions.

(6) Effect of overvoltage on side streamer (SS): overvoltage provides a higher background field $(E/N)_b$ for the prop-

agation of the primary streamer. When $(E/N)_b \leq 225$ Td, it is insufficient to sustain continuous propagation, and the SS merging remains the dominant factor facilitating breakdown. When $(E/N)_b \approx 235$ Td, SS no longer plays a dominant role and acts only supportively. When $(E/N)_b \geq 245$ Td, SS no longer appears, indicating its role negligible.

ACKNOWLEDGMENT

The authors gratefully acknowledge the funding support from the National Natural Science Foundation of China (Contract No. 52277154). Z. Feng thanks Researcher Dr. Peng Wang and Caomingzhe Si from the Department of Electrical Engineering, Tsinghua University, for fruitful discussions.

AUTHOR DECLARATIONS

Conflict of Interest. The authors have no conflicts to disclose.

DATA AVAILABILITY

The data that support the findings of this study are available from the corresponding author upon reasonable request.

-
- [1] J. Wang, Q. Hu, Y. Chang, J. Wang, R. Liang, Y. Tu, C. Li, and Q. Li, *CSEE J. Power Energy Syst.* **7**, 1011 (2021).
- [2] C. Li, C. Zhang, J. Lv, F. Liang, Z. Liang, X. Fan, U. Riechert, Z. Li, P. Liu, J. Xue, C. Pan, G. Chen, L. Zhang, Z. Wang, W. Lu, H. Liang, Z. Pan, W. Zhuang, G. Mazzanti, D. Fabiani, B. Liu, S. Cao, J. Zhong, Y. Deng, Z. Nan, J. Tang, and J. He, *iEnergy* **1**, 400 (2022).
- [3] J. R. Laghari and A. H. Qureshi, *IEEE Trans. Electr. Insul.* **EI-16**, 388 (1981).
- [4] H. Kuwahara, S. Inamura, T. Watanabe, and Y. Arahata, *IEEE Trans. Power App. Syst.* **PAS-93**, 1546 (1974).
- [5] L. Donzel, M. Seeger, D. Over, and J. Carstensen, *Energies* **15** (2022).
- [6] S. Xiao, X. Zhang, R. Zhuo, D. Wang, J. Tang, S. Tian, and Y. Li, *IEEE Trans. Dielectr. Electr. Insul.* **24**, 2299 (2017).
- [7] A. Diessner and J. G. Trump, *IEEE Trans. Power App. Syst.* **PAS-89**, 1970 (1970).
- [8] H. You, Q. Zhang, C. Guo, P. Xu, J. Ma, Y. Qin, T. Wen, and Y. Li, *IEEE Trans. Dielectr. Electr. Insul.* **24**, 876 (2017).
- [9] J. Ma, Q. Zhang, Z. Wu, C. Guo, T. Wen, G. Wang, and C. Gao, *IEEE Trans. Dielectr. Electr. Insul.* **25**, 1439 (2018).
- [10] J. Wang, Q. Li, B. Li, C. Chen, S. Liu, and C. Li, *IEEE Trans. Dielectr. Electr. Insul.* **23**, 1951 (2016).
- [11] X. Li, X. Hu, H. Xu, P. Jiang, M. Wu, B. Niu, Z. Li, and Q. Zhang, *IEEE Trans. Power Deliv.* **38**, 4039 (2023).
- [12] W. Zhong, Y. Shi, C. Zhang, and X. Li, *IEEE Trans. Dielectr. Electr. Insul.* **27**, 1095 (2020).
- [13] Y. Shi, W. Zhong, A. Xu, and P. Gan, *IEEE Trans. Plasma Sci.* **49**, 813 (2021).
- [14] Q. Sun, Q. hong Zhou, W. Yang, Y. Dong, H. tian Zhang, M. meng Song, and Y. Wu, *Plasma Sources Sci. Technol.* **30**, 045001 (2021).
- [15] N. Lebedev and I. Skalskaya, *Sov. Phys. Tech. Phys.*, 268 (1962).
- [16] Z. Feng, Y. Jiang, L. Zhang, Z. Liu, K. Wang, X. Wang, X. Zou, H. Luo, and Y. Fu, *Appl. Phys. Lett.* **125**, 134101 (2024).
- [17] R. T. Waters, *J. Phys. D: Appl. Phys.* **52**, 025203 (2018).
- [18] M. Seeger and M. Clemen, *J. Phys. D: Appl. Phys.* **47**, 025202 (2013).
- [19] I. D. Chalmers, I. Gallimberti, A. Gibert, and O. Farish, *Proc. R. Soc. Lond. A* **412**, 285–308 (1987).
- [20] M. Seeger, L. Niemeyer, and M. Bujotzek, *J. Phys. D: Appl. Phys.* **42**, 185205 (2009).
- [21] A. H. Cookson, *IEE Proc. A Sci. Meas. Technol.* **128**, 303 (1981).
- [22] A. H. Cookson, O. Farish, and G. M. L. Sommerman, *IEEE Trans. Power App. Syst.* **PAS-91**, 1329 (1972).
- [23] A. H. Cookson and O. Farish, *IEEE Trans. Power App. Syst.* **PAS-92**, 871 (1973).
- [24] C. Cooke, R. Wootton, and A. Cookson, *IEEE Trans. Power App. Syst.* **96**, 768 (1977).
- [25] I. Gallimberti and N. Wiegart, *J. Phys. D: Appl. Phys.* **19**, 2363 (1986).
- [26] Z. Zhao, Z. Dai, A. Sun, and J. Li, *High Volt.* **7**, 382 (2022).
- [27] Z. Zhao, Z. Huang, X. Zheng, C. Li, A. Sun, and J. Li, *Plasma Sources Sci. Technol.* **31**, 075006 (2022).
- [28] Z. Wu, Q. Zhang, L. Zhang, C. Guo, Q. Du, and L. Pang, *Plasma Sources Sci. Technol.* **28**, 085018 (2019).

- [29] Z. Feng, X. Wang, X. Zou, H. Luo, and Y. Fu, [arXiv preprint, arXiv:2409.19646](#) (2024).
- [30] X. Meng, W. Zhuang, L. Lin, H. Li, Z. Cao, and H. Mei, [IEEE Trans. Dielectr. Electr. Insul.](#), **1** (2024).
- [31] Q. Gao, C. Niu, X. Wang, A. Yang, Y. Wu, A. B. Murphy, M. Rong, X. Fu, J. Liu, and Y. Xu, [J. Phys. D: Appl. Phys.](#) **51**, 295202 (2018).
- [32] L. Zhang, Z. Liu, Y. Guo, J. Liu, K. Wang, H. Luo, and Y. Fu, [Plasma Sources Sci. Technol.](#) **33**, 025001 (2024).
- [33] D. Levko and Y. E. Krasik, [J. Appl. Phys.](#) **111**, 013305 (2012).
- [34] D. Levko, V. Tz. Gurovich, and Y. E. Krasik, [J. Appl. Phys.](#) **111**, 123303 (2012).
- [35] Z. Xiong and M. J. Kushner, [Plasma Sources Sci. Technol.](#) **23**, 065041 (2014).
- [36] Y. Guo and S. Nijdam, [Plasma Sources Sci. Technol.](#) **33**, 045006 (2024).
- [37] Z. Wang, S. Dijcks, Y. Guo, M. van der Leege, A. Sun, U. Ebert, S. Nijdam, and J. Teunissen, [Plasma Sources Sci. Technol.](#) **32**, 085007 (2023).
- [38] X. Li, S. Dijcks, A. Sun, S. Nijdam, and J. Teunissen, [Plasma Sources Sci. Technol.](#) **33**, 095009 (2024).
- [39] Z. Wang, A. Sun, S. Dujko, U. Ebert, and J. Teunissen, [Plasma Sources Sci. Technol.](#) **33**, 025007 (2024).
- [40] B. Guo, U. Ebert, and J. Teunissen, [Plasma Sources Sci. Technol.](#) **32**, 115001 (2023).
- [41] R. Marskar, [J. Comput. Phys.](#) **504**, 112858 (2024).
- [42] R. Marskar, [Plasma Sources Sci. Technol.](#) **33**, 025023 (2024).
- [43] D. Levko and L. L. Raja, [J. Appl. Phys.](#) **133**, 053301 (2023).
- [44] Y. Zhu, X. Chen, Y. Wu, J. Hao, X. Ma, P. Lu, and P. Tardiveau, [Plasma Sources Sci. Technol.](#) **30**, 075025 (2021).
- [45] N. Y. Babaeva and M. J. Kushner, [Plasma Sources Sci. Technol.](#) **18**, 035009 (2009).
- [46] N. Y. Babaeva and M. J. Kushner, [Plasma Sources Sci. Technol.](#) **18**, 035010 (2009).
- [47] L. G. Christophorou and J. K. Olthoff, [J. Phys. Chem. Ref. Data](#) **29**, 267 (2000).
- [48] G. J. M. Hagelaar and L. C. Pitchford, [Plasma Sources Sci. Technol.](#) **14**, 722 (2005).
- [49] R. Van Brunt and J. Herron, [IEEE Trans. Electr. Insul.](#) **25**, 75 (1990).
- [50] F. Zeng, M. Zhang, D. Yang, and J. Tang, [Plasma Chem. Plasma Process.](#) **39**, 205 (2019).
- [51] D. Levko and L. L. Raja, [Plasma Sources Sci. Technol.](#) **26**, 035003 (2017).
- [52] M. B. Zhelezniak, A. K. Mnatsakanian, and S. V. E. Sizykh, [High Temp. Sci.](#) **20**, 357 (1982).
- [53] A. Bourdon, V. P. Pasko, N. Y. Liu, S. Célestin, P. Ségur, and E. Marode, [Plasma Sources Sci. Technol.](#) **16**, 656 (2007).
- [54] A. Luque, U. Ebert, C. Montijn, and W. Hundsdorfer, [Appl. Phys. Lett.](#) **90**, 081501 (2007).
- [55] R. Morrow, [IEEE Trans. Plasma Sci.](#) **14**, 234 (1986).
- [56] M. S. Bhalla and J. D. Craggs, [Proc. Phys. Soc.](#) **80**, 151 (1962).
- [57] L. E. Kline, D. K. Davies, C. L. Chen, and P. J. Chantry, [J. Appl. Phys.](#) **50**, 6789 (1979).
- [58] H. Boyd and G. Crichton, [Proc. Inst. Electr. Eng.](#) **118**, 1872 (1971).
- [59] V. N. Maller and M. S. Naidu, [IEEE Trans. Plasma Sci.](#) **3**, 205 (1975).
- [60] T. Yoshizawa, Y. Sakai, H. Tagashira, and S. Sakamoto, [J. Phys. D: Appl. Phys.](#) **12**, 1839 (1979).
- [61] J. P. Novak and M. F. Fréchette, [J. Appl. Phys.](#) **55**, 107 (1984).
- [62] M. C. Siddagangappa, C. S. Lakshminarasimha, and M. S. Naidu, [J. Phys. D: Appl. Phys.](#) **15**, L83 (1982).
- [63] K. B. M. Jr and D. Edelson, [Proc. Phys. Soc.](#) **81**, 382 (1963).
- [64] S. Abdul Madhar, P. Mraz, A. Rodrigo Mor, and R. Ross, [Int. J. Electr. Power Energy Syst.](#) **118**, 105733 (2020).
- [65] P. Wenger, M. Beltle, S. Tenbohlen, U. Riechert, and G. Behrmann, [IEEE Trans. Power Deliv.](#) **34**, 1540 (2019).
- [66] D. Fahmi, H. A. Illias, H. Mokhlis, and I. M. Y. Negara, [IEEE Trans. Dielectr. Electr. Insul.](#) **30**, 658 (2023).
- [67] H. Ji, C. Li, Z. Pang, G. MA, X. Cui, W. Zhao, and J. Wang, [IEEE Trans. Dielectr. Electr. Insul.](#) **24**, 259 (2017).
- [68] H. Ji, C. Li, Z. Pang, G. Ma, X. Cui, Z. Zeng, and Z. Rong, [IEEE Trans. Dielectr. Electr. Insul.](#) **23**, 3355 (2016).
- [69] Y. Wang, R. L. Champion, L. D. Doverspike, J. K. Olthoff, and R. J. Van Brunt, [J. Chem. Phys.](#) **91**, 2254 (1989).
- [70] R. J. Van Brunt and M. Misakian, [IEEE Trans. Electr. Insul. EI-17](#), 106 (1982).
- [71] M. Seeger, L. Niemeyer, and M. Bujotzek, [J. Phys. D: Appl. Phys.](#) **41**, 185204 (2008).
- [72] S. Mirpour and S. Nijdam, [Plasma Sources Sci. Technol.](#) **31**, 105009 (2022).
- [73] A. Abahazem, N. Merbahi, O. Ducasse, O. Eichwald, and M. Yousfi, [IEEE Trans. Plasma Sci.](#) **36**, 924 (2008).
- [74] R. Ono and T. Oda, [J. Phys. D: Appl. Phys.](#) **36**, 1952 (2003).
- [75] Y. Li, E. M. van Veldhuizen, G. J. Zhang, U. Ebert, and S. Nijdam, [Plasma Sources Sci. Technol.](#) **27**, 125003 (2018).
- [76] A. Komuro, R. Ono, and T. Oda, [Plasma Sources Sci. Technol.](#) **22**, 045002 (2013).
- [77] A. Luque, V. Ratushnaya, and U. Ebert, [J. Phys. D: Appl. Phys.](#) **41**, 234005 (2008).
- [78] Z. Zhao, Z. Wang, Z. Duan, and Y. Fu, [IEEE Trans. Dielectr. Electr. Insul.](#), **1** (2024).
- [79] Z. Liu, Y. Hirakawa, K. Yamamoto, T. Ryu, J. Li, N. Jiang, T. Namihira, and D. Wang, [Plasma Sources Sci. Technol.](#) **33**, 095001 (2024).
- [80] F. Wang, K. Liang, L. Zhong, S. Chen, T. Wan, X. Duan, and X. Dong, [IEEE Trans. Dielectr. Electr. Insul.](#) **30**, 1154 (2023).
- [81] S. Wang, Y. Xu, and F. Lü, [IEEE Trans. Dielectr. Electr. Insul.](#) **31**, 75 (2024).